

Article

Fractal Features in kHz Electromagnetic Observations Preceding Near-Field Earthquakes in Ilia, Greece

Dimitrios Nikolopoulos ^{1,*} , Ermioni Petraki ¹ , Muhammad Rafique ² , Aftab Alam ³ , Demetrios Cantzos ¹  and Panayiotis Yannakopoulos ⁴ 

¹ Department of Industrial Design and Production Engineering, University of West Attica, Petrou Ralli & Thivon 250, GR-12244 Aigaleo, Greece; ermionipetraki@gmail.com (E.P.); cantzos@uniwa.gr (D.C.)

² Department of Physics, University of Azad Jammu and Kashmir Muzaffarabad, King Abdullah Campus, Azad Kashmir 13100, Pakistan; mrafique@ajku.edu.pk

³ Centre for Earthquake Studies, National Centre for Physics, Shahdra Valley Road, P.O. Box No. 2141, Islamabad 44000, Pakistan; aftab.alam@ncp.edu.pk

⁴ Department of Informatics and Computer Engineering, University of West Attica, Agiou Spyridonos, GR-12243 Aigaleo, Greece; pyannakopoulos@yahoo.co.uk

* Correspondence: dniko@uniwa.gr; Tel.: +30-210-5381338

Abstract: This paper reports kHz EM observations recorded by the Kardamas station in Ilia, Greece a few days before four near-field earthquakes occurred within a 24 km radius, with epicentral depths below 29 km. This work investigated the fractal features hidden in the EM observations via power-law analysis. All EM signals exhibited characteristic fractal epochs with organisation in space and time. A significant number of accurate fractal segments were delineated in the majority of the EM observations. A significant number of fractal areas corresponded to predictable Class I fBm category with $1 \leq b \leq 3$ ($0 \leq H \leq 1$). Numerous persistent key-periods are reported with $2 < b \leq 3$ ($0.5 \leq H \leq 1$) which are deemed as signs of impending earthquakes according to the literature. Numerous segments were found with strong persistent b -values in the range ($2.3 \leq b \leq 3$) ($0.65 \leq H \leq 1$) and b -values corresponding to switching between antipersistence and persistence with ($1.7 \leq b < 2.3$) ($0.35 \leq H < 0.65$). These are deemed as the most significant precursory signs. Interpretations are given via the asperity model.

Keywords: earthquakes; electromagnetic observation; fractal analysis; power-law



Citation: Nikolopoulos, D.; Petraki, E.; Rafique, M.; Alam, A.; Cantzos, D.; Yannakopoulos, P. Fractal Features in kHz Electromagnetic Observations Preceding Near-Field Earthquakes in Ilia, Greece. *Geosciences* **2023**, *13*, 387. <https://doi.org/10.3390/geosciences13120387>

Academic Editors: Masashi Hayakawa and Jesus Martinez-Frias

Received: 8 November 2023

Revised: 7 December 2023

Accepted: 8 December 2023

Published: 15 December 2023



Copyright: © 2023 by the authors. Licensee MDPI, Basel, Switzerland. This article is an open access article distributed under the terms and conditions of the Creative Commons Attribution (CC BY) license (<https://creativecommons.org/licenses/by/4.0/>).

1. Introduction

Earthquakes are particularly disastrous natural catastrophes that may cause substantial damages of life and property. The enormous amount of energy released by an earthquake has devastating effects on urban residents, especially if the earthquake's epicentre is nearby. Although catastrophic earthquakes are inevitable as a result of natural events, it is extremely difficult to predict them. Therefore, one of science's greatest challenges is the search for reliable seismic precursors [1–8]. According to Conti et al. [9], the question of earthquake prediction is still unresolved.

Earthquakes are complex and, thus, advanced methodologies are needed [6]. The corresponding forecast effort requires focusing the estimation of event time, location, and magnitude on regions where strong earthquakes are possible [1]. Among the various precursors (reviews, [3,6,8,10]), electromagnetic (EM) observations can be effective in signalling the occurrence of imminent earthquakes. The related frequency range includes bands from 0.001 Hz to 1 Hz (ultra low frequencies—ULF) [11–25], between 1 kHz and 10 kHz (low frequencies—LF) [26–33], between 40 MHz and 60 MHz (high frequencies—HF) [28,30–32,34,34–36] and up to 300 MHz (very high frequencies—VHF) [11,36,37]. The EM variations are recorded by ground stations [17–20,27,31,38–45], remote sensory devices [46,47] and satellites [36,48].

This paper focuses on *kHz* EM observations recorded by a ground-station located in Kardamas (21.34° E, 37.76° N), Ilia, Greece (Figure 1a). Among the various earthquakes that occurred in Ilia, in four earthquakes (Table 1, Figure 2): (a) the epicentral distance was below 24 km from Kardamas; (b) the epicentral depth was below 29 km, i.e., it was roughly near the surface; (c) the visual inspection of the *kHz* signals provided at least one or more unusual EM patterns; and (d) analysis has been implemented with at least one fractal method (see available methodologies, for example, in references [30,35,49,50]). The reader should note that there are several difficulties in remotely operating a station 280 km away from the university facilities. The lengthy experience with the Kardamas EM station has shown that various types of disturbances occur which result in errors in measurements. Examples are the failures in electronics, various types of errors in data-logger communication, network loss and, most importantly, sudden AC voltage variations or stops and usual lightning strikes [31]. The reader should note, also, that even for continuous *kHz* EM observations free from measurement errors, it is not usual to have earthquakes with the combination of the aforementioned (a–c). This is because a significant amount of time is required everyday, to download the data, to graph the EM observations in a computer, to check the data of each channel in detail and, then, to search the earthquake database for near earthquakes. For the best cases, the investigation with at least one fractal method is also very time consuming, for software running, results organisation and data storage, not accounting for the time spent for software development [35]. The above facts justify, therefore, why it is very difficult to find earthquakes as those of Table 1 and Figure 2, and provide sufficient evidence for the significance of the dataset within this paper.

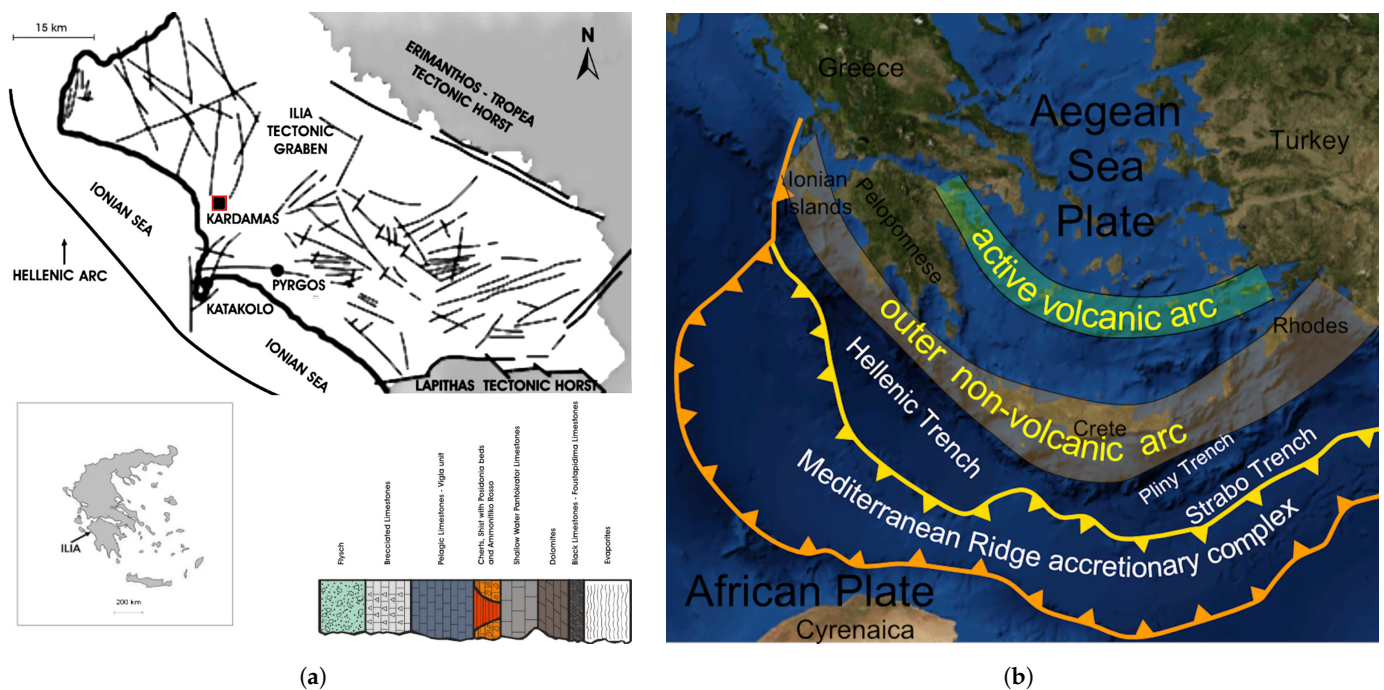


Figure 1. Geology of the area of study. (a) Kardamas position and the geotectonic map of Ilia with the most important faults and the stromatografic evolution of the Ionian Zone; (b) The geological background of Greece. The yellow and orange seismic plates that encompass Greece and the Trenches are seen in the figure.

The EM variations of this paper are analysed with the power-law spectral fractal analysis (hereafter called power-law analysis). According to several publications (e.g., [16,20,31,51,52], and reported references), this technique is very reliable for unfolding the fractal features hidden in the time-series. The motivation is to determine whether persistent fractal patterns exist in portions of the recorded EM time series that can be regarded as precursory indicators of the forthcoming earthquakes. The EM segments of

enhanced precursory value are found and separated from those of limited predictability. Models of potential geological sources are discussed.

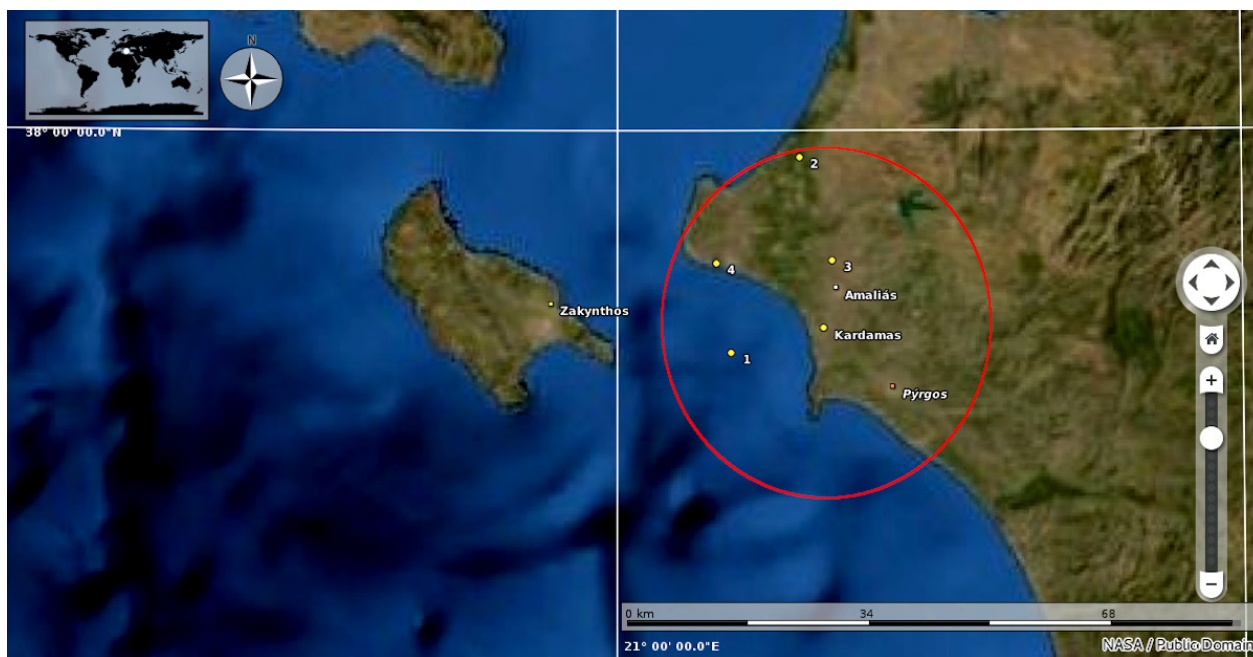


Figure 2. The epicentres of the earthquakes in Table 1 occurred within 24 km radius (red circle) centred at the Kardamas station (21.34° E, 37.76° N). The identifiers are according to Table 1.

Table 1. Earthquakes included in the present study in chronological sequence. The actual dates of the earthquake and the corresponding Julian Day (JD) of each year are also given. Abbreviations: M_L : Local Magnitude, Lt: Latitude, Lg: Longitude, Depth: Epicentral depth, Dist: Distance of the earthquake epicentre from the Kardamas station. All data, except symbol and JD, are retrieved from [53].

i	Symbol	Date	GMT	JD	M_L	Lt (°N)	Lg (°E)	Depth (km)	Dist (km)
1.	EQ1	2019/02/04	17:41:09	035	4.3	37.72	21.18	26.4	13.3
2.	EQ2	2018/07/05	21:39:05	188	4.5	37.97	21.29	9.2	24.0
3.	EQ3	2015/08/30	13:28:02	242	4.4	37.83	21.34	27.0	9.6
4.	EQ4	2015/12/12	08:34:09	346	4.5	37.83	21.16	28.9	17.5

2. Experimental Aspects

2.1. Geology and Seismic Significance of the Area

The EM measurement site (Kardamas, Ilia, south-west Greece, Figure 1a) is located on a large depression structure (graben) very close to the convergent boundary between the European and African tectonic plates (Figure 1b). The underlying geology consists of Mesozoic-early Cenozoic carbonate rocks that were initially deposited on a number of zones (pre-Apulian and Gavrovo) and basins (Ionian and Pindos). These carbonate rocks are dispersed along thrust faults that strike north-south, dip east and are spread upward and westward into subordinate flysch deposits [54,55]. The Mt. Lapithas horst, Mt. Erymanthos horst and Tropea horst (Figure 1a), all of which are composed of Alpine formations, encircle the Ilia graben on the south, east and north, respectively. These horsts’ single fault zones have distinct morphological discontinuities that can be used to locate their limits. The entire area is a part of the Pyrgos graben, which is bounded by two faults that run in opposite directions, NW-SE and NNE-SSW. The graben comprises outcropping alpine strata (Ionian zone) and is marked by co-sedimentation tectonism. The Inoi Formation, the Peristeri, the Vounargo, Keramidia, Erymanthos Formation, the Katakolo Formation, Alluvial Deposits, Coastal, Marsh Deposits and Dunes are among the eleven distinct geological formations

found in the Iliia graben. Kardamas, a cohesive porous calcitic sandstone that is a member of the Katakolo formation, may contain coarse rock fragments from a variety of different rock types. Its age is Upper Pleistocene, its thickness spans from 2 to 10 m, and it largely surrounds Katakolo [55,56]. The highest layer consists, according to hydro-geological drillings, of recent deposits of soft to medium density clayey sands, sandy clays of medium cohesiveness, sandy clays of medium plasticity regionally with gravel, thin layers of silt, and soft layers of flexible clay. Additionally, Kardamas and Iliia are situated in the outermost part of the Hellenic trench (Figure 1b). Iliia is associated with noteworthy active seismic structures and significant earthquakes because of its location at the convergence of the Eurasian, African, Aegean Sea and Anatolian plates. The location and geology of Iliia and Kardamas make the EM observation site important for examining tectonic activity [56]. Iliia produced more than 600 earthquakes with local magnitudes greater than 4.0, 6 of which were extremely damaging [53,57]. The site is an easily accessible flat area far from artificial strain and irrigation but near a city, which is important when changes and corrections of the electronics are needed.

2.2. Instrumentation

The electromagnetic disturbances are continuously monitored by the Kardamas station via

- (i) Circular magnetic field antennas synchronised properly at 3 kHz and at 10 kHz. Two orientations are installed. One at the east-west (EW) orientation and the other to the north-south (NS) orientation.
- (ii) Campbell CR-10 data-logger with a 2 h buffer.
- (iii) Telemetry equipment continuously sending the measurements to a personal computer at the rate of 1 Hz.

3. Mathematical Aspects

3.1. Power-Law Analysis

There are many different natural physical systems that can be described by fractals. When the entire system, or a section of it, is translated, rotated, stressed or compressed in space, the characteristic fractal behaviour is observed. Depending on how the changes are mathematically defined, the system is either categorised as self-affine or self-similar. Self-affine and self-similar physical systems are fractals because each of their constituent pieces is either a little or big replica of the whole, but at different scales. Therefore, by concentrating on their scaled components, fractal systems may be investigated. A fractal system's long-memory [58–61], complexity [59,62–65] and scaling features are all intimately connected to one another. For example, one may evaluate a system's long memory by looking at the complexity of the system, and vice versa [50,66]. These features reveal how closely a system's history, present and future are interconnected. Especially before earthquakes, the space and time associations become complex and long-lasting [26] and the underlying seismic system evolves naturally to self-organised critical (SOC) states with fractal organisation [20]. This progression creates seismic tracks in earthquake hazard systems [26] which may unfold with fractal methods [16,20,24,26,51,52,67,68]. The evolution of fractals can describe different stages to the final catastrophe [16,20,52,67].

One of the most reliable technique for analysing the fractal patterns in a seismic system is the power-law analysis. This is because space-time fractals follow power-laws associated with the different scales [16,20,26,27,30,31,51,52,67,68]. A very significant tool in this analysis is the power spectral density (PSD). The PSD provides information concerning the contribution of each frequency within the investigated time-series according to Equation (1) [31]

$$S(f) = \lim_{T \rightarrow \infty} E\left[\frac{|W_T(f)|^2}{T}\right] \quad (1)$$

where the transform $W_T(f)$ is used. For digital signals, $W_T(f)$ is often the fast Fourier transform. The reader should keep in mind that the Fourier transform may not be appro-

appropriate when slow and fast signal variations coexist, since the time-frequency resolution of the FFT is fixed. In comparison, the continuous wavelet transform (CWT) has a variable time-frequency resolution and can better analyse transient or non-stationary signals. The reader should note here, in relation, that the continuous wavelet transform was employed almost 20 years ago, in the analysis of earthquake precursory signals by means of the wavelet transform modulus maxima method [69]. The CWT that was used in this paper is given by Equation (2) [31]

$$C(a, b; f(t), \psi(t)) = \int_{-\infty}^{\infty} f(t) \left(\frac{1}{a} \psi^* \left(\frac{t - ba}{a} \right) dt \right) \quad (2)$$

where a is the scale ($a > 0$), b is a position inside the signal, ψ is the wavelet-base function, $C(a, b)$ are the coefficients of CWT and $*$ is the complex conjugate. The coefficients of the CWT are influenced by the scale, position and the wavelet used. The CWT coefficients $C(a, b)$ are produced by continuously altering the values of the scale parameter, a , and the position parameter, b . The Morlet wavelet utilised here is given by Equation (3) [31]:

$$\psi(t) = \frac{1}{\sqrt{\pi B}} e^{-\frac{t^2}{B}} e^{i2\pi C t} \quad (3)$$

where B is the bandwidth of the frequencies of the Fourier Transform of the wavelet function at t , C is the central frequency of the Fourier Transform of the wavelet function at t and i is the notation for the imaginary part of the exponent.

Fractals follow a power-law of the form of Equation (4) with PSD, $S(f)$ [16,31,35]

$$S(f) = a \cdot f^{-b} \quad (4)$$

where f is the central frequency C of the Morlet wavelet of Equation (2). The power-law PSD f dependency is a straight line in the conversion $\log(S(f)) - \log(f)$. The spectral amplification a is the line's intercept, while the power-law scaling exponent b is the line's slope. b measures the intensity of the power-law correlations, and the amplification a is the strength of the spectral components f that obey the power law.

3.1.1. Application of Power-Law Analysis

The next steps are followed for the power-law analysis of the seismic series under investigation:

1. The EM time-series is divided into segments (windows). In accordance with the previous papers, the segmentation is set to 1024 samples per window.
2. The PSD of the EM signal is calculated in each discrete window utilising the CWT with the Morlet base wavelet.
3. The PSD is checked for power-law $S(f) = a \cdot f^{-b}$ trends of Equation (4), in each segment, by utilising as frequency (f) the central frequency of the Fourier transform of each Morlet wavelet of Equation (3) at the corresponding scale (C). This is implemented via a least square fit to the linear transformation $\log(S(f)) - \log(f)$ of (4). Accurate fractal segments are considered those with the square of Spearman's correlation coefficient, $r^2 \geq 0.95$ of the linear fit.
4. Each window advances one sample forward and the steps (1)–(3) are repeated to the end of the time series.
5. Plots of power-law b and $\log a$ with time are produced and the partial results were extracted to ASCII files for further use.

A similar approach has been employed in EM and radon time series (e.g., [30–33]).

3.2. Further Issues

3.2.1. Hurst Exponent

To find long-lasting links in time or space, a parameter called the Hurst exponent (H) can be utilised [70,71]. The Hurst exponent can determine the evolution of fractals and the

roughness of the associated profiles [26,35,72]. The Hurst exponent has been used in many different areas, including hydrology [70,71]), astrophysics and applications [73,74], noisy observations of traces in traffic [75–77], climatic dynamics [78], seizures prior to epilepsy [79–81], processes of capital markets [82–85] and precursory series before impending earthquakes (e.g., [24,31,35]).

The Hurst exponent provides important details [13,35,86]:

1. If $0.5 < H \leq 1$, the series are persistent. A series' high value is followed by another high value and a series low value is followed by another low value. The tendencies are long-lasting and occur in the series' far future.
2. If $0 \leq H < 0.5$, the series are antipersistent. Low series' values follow high values and vice versa. There is an continuous exchange between low and high values for low H values in the series' future.
3. If $H = 0.5$, associated series are random.

For the fractional Brownian (fBm) category, the Hurst exponent can be calculated from power-law exponents b as

$$H = 0.5 \cdot (b - 1) \quad (5)$$

whereas for the fractional Gaussian (fGn) category:

$$H = 0.5 \cdot (b + 1) \quad (6)$$

It should be noted that the Hurst exponent values calculated by Equation (5) may deviate from the H -values calculated by other methods from in situ measurements. This is because Equation (5) is based on simple linear approximations. In the actual case, the relation between H and b is an increasing function but of a different type [31].

3.2.2. Class Segmentation

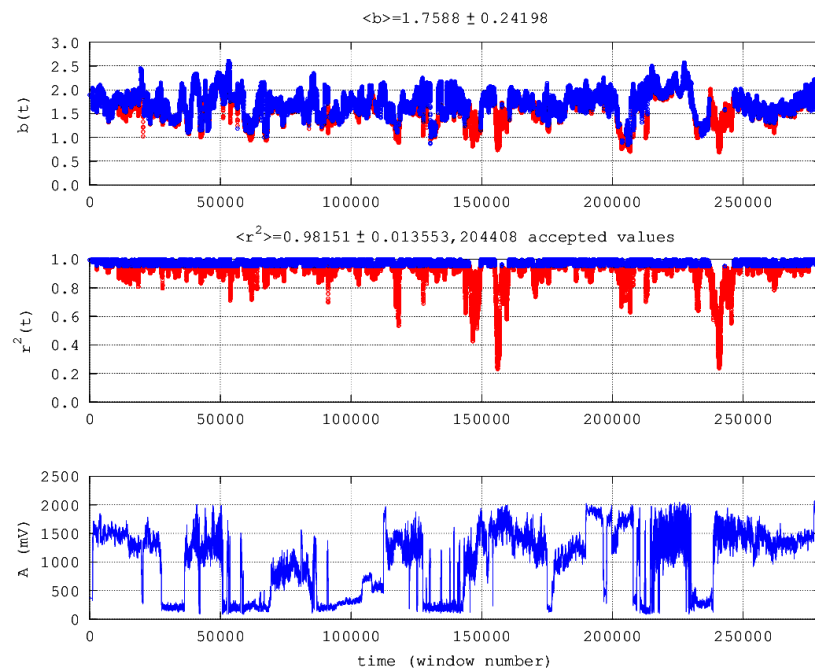
To further organise the findings from the power-law analysis, two classes are created:

- (a) Class I: This class contains the EM segments that exhibit least square log-log fits with Spearman's coefficient of $r^2 \geq 0.95$ and, simultaneously, power-law exponents between $1 \leq b \leq 3$ ($0 \leq H \leq 1$). These segments are modelled by the fBm category [30,51]. Especially, the Class I EM segments with:
 - Antipersistency-persistency increment changes with b exponents between ($1.7 \leq b < 2.3$) ($0.35 \leq H < 0.65$) and ($2.3 \leq b \leq 3$) ($0.65 \leq H \leq 1$) are of significant precursory value (e.g., [30,31], and references therein);
 - Pure persistent power-law exponents ($2 < b \leq 3$) ($0.5 < H \leq 1$) are considered by others (e.g., [16,26,51,67,68], and references therein) as signs of the inevitable occurrence of ensuing earthquakes;
 - If $b = 2$ ($H = 0.5$), there is no correlation between process increments and the associated geo-system follows random paths driven by non-memory dynamics (random-walk);
 - If $b = 1.0$ ($H = 0$), the fluctuations of the processes do not grow and the signal is stationary.
- (b) Class II: This class contains the EM segments with (A) Spearman's $r^2 < 0.95$ or (B) $r^2 \geq 0.95$ and $-1 \leq b < 1$ ($0 \leq H < 1$), i.e., accurate fractals that follow the fGn category. The Class II EM segments are of low precursory value and low predictability (e.g., [27]).

4. Results and Discussion

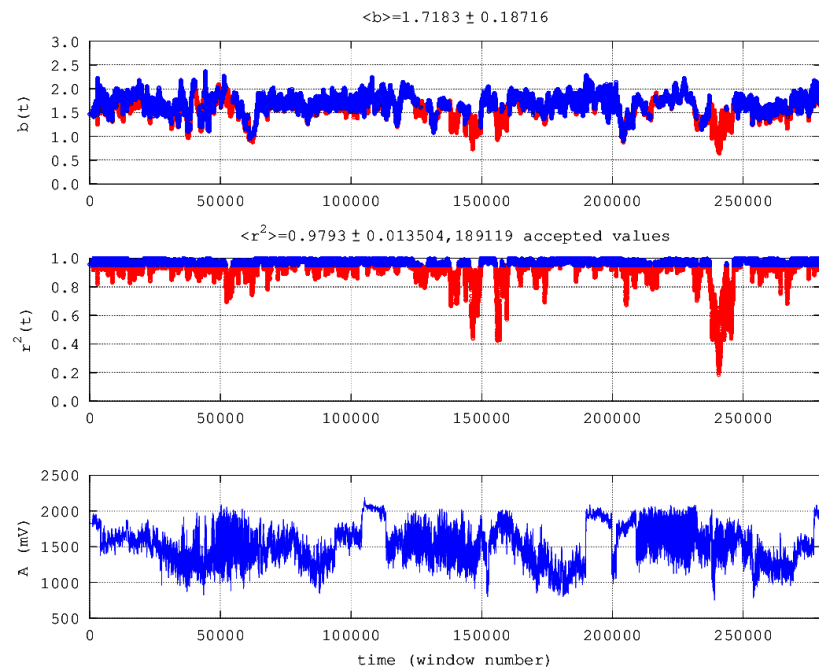
Figures 3–7 present results from the power-law method. In all of these figures, the EM measurements sampling rate is 1 s^{-1} . The time profile of the power-law b -exponent is very different from the corresponding profile of the EM observations. This is because the power-law method identifies the long-lasting associations and the fractal tendencies that are hidden in time series [20,27,30,31,37]. In Figures 3–6, important key-periods

can be recognised which exhibit strong persistency with $2.3 \leq b \leq 3.0$ or switching between antipersistency and persistency with $1.7 \leq b < 2.3$. According to several references (e.g., [27,29,35,87], and especially references therein), these key periods correspond to predictable Class I segments that have been characterised as signs of precursory activity. As mentioned in Section 3.2.2, others claim that the segments between $2 < b \leq 3$ (especially for kHz EM observations) signalise the inevitable occurrence of earthquakes [16,26,51,67,68]. The former areas (but also the latter ones) are associated with long-range temporal dependencies, namely, the strong system's memory. This means that each series' value correlates not only to the most recent series' value but also to the series' long-term history, importantly, in a scale-invariant, fractal manner (e.g., [26,35,68]). Hence, the system that generates the EM observations not only has its history defining its presence, but most importantly, both define its future (non-Markovian behaviour) and, significantly, in a long-term manner [35]. The above suggest that internal system's dynamics are controlled by positive feedback and, as a result, external influences can easily lead the system out of equilibrium [88]. Consequently, the system develops a self-regulating nature and, to a large part, the feature of irreversibility, which is one of the crucial elements of predictability [89]. From a different angle, this behaviour indicates that several processes acting on various scales have an impact on the eventual result of fracture [20,29,35,39]. Moreover, it may be well-hypothesised that the progression of the Earth's crust towards fracture is a Self Organised Critical (SOC) phenomenon [3,20,52] and the last stage of the evolution of earthquake generation [16,26,35,51,67,68], but see also Varotsos et al. [90].

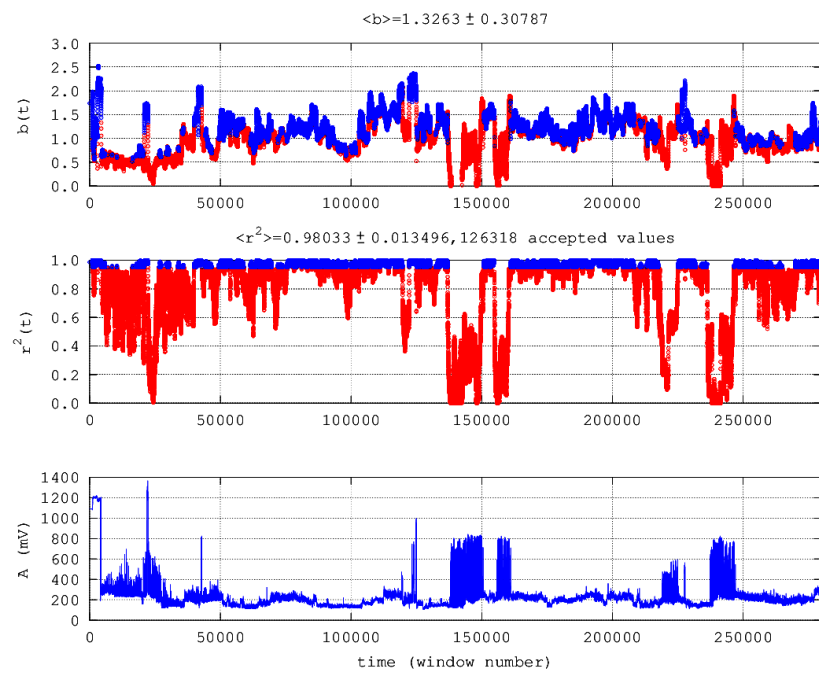


(a) Frequency 3 kHz—EW antenna orientation

Figure 3. Cont.

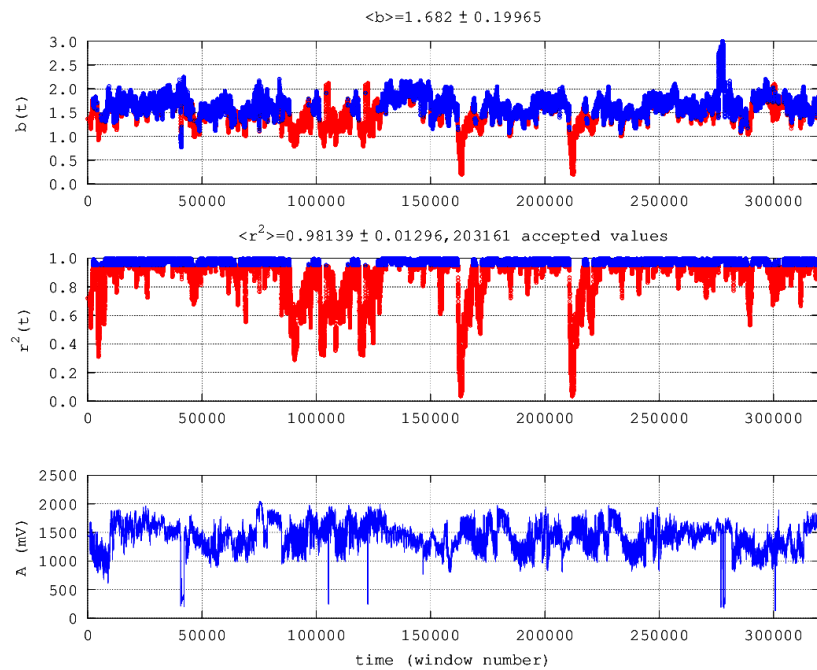


(b) Frequency 3 kHz—NS antenna orientation

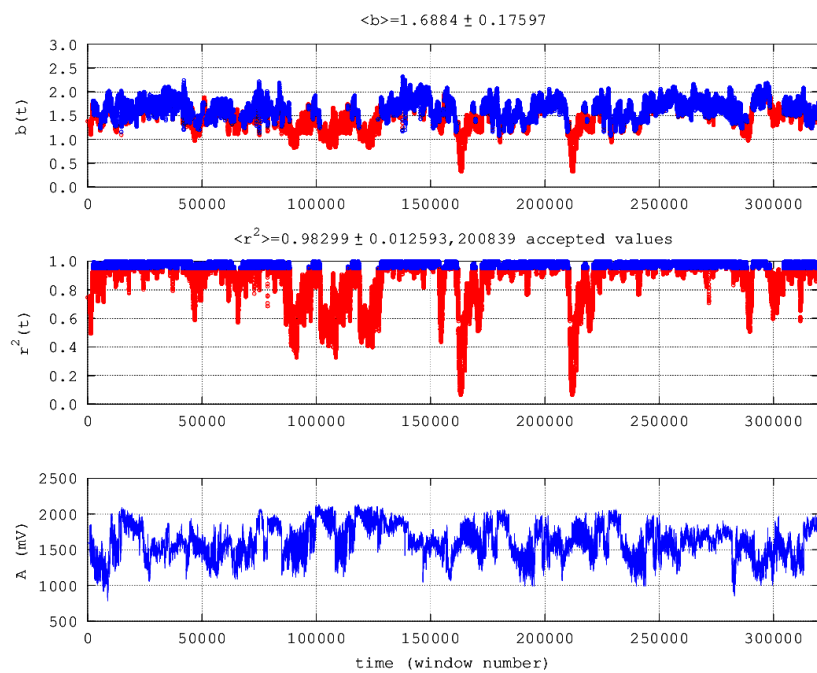


(c) Frequency 10 kHz—EW antenna orientation

Figure 3. Results from power-law analysis. Year 2019, kHz EM observations from JD 31 to JD 35 (EQ1 occurred on JD 35, Table 1). From bottom to top: **(bottom)** The EM observations of amplitude A ; **(middle)** The square of Spearman’s correlation coefficient (r^2) in every 1024 window; **(top)** The evolution of power-law b -exponent ($b(t)$). The horizontal axis is measured in window number starting from the beginning of measurements (JD = 31, time = 00:00:00). Last window is omitted. The number of each window coincides with the actual EM measurement time in s (Section 3.1.1, sliding of step 1). Blue areas are accurate fractals ($r^2 \geq 0.95$). Red areas are non-fractal. The averages of b ($\langle b \rangle$) and r^2 ($\langle r^2(t) \rangle$) in accurate fractal areas are given \pm the corresponding standard deviations.

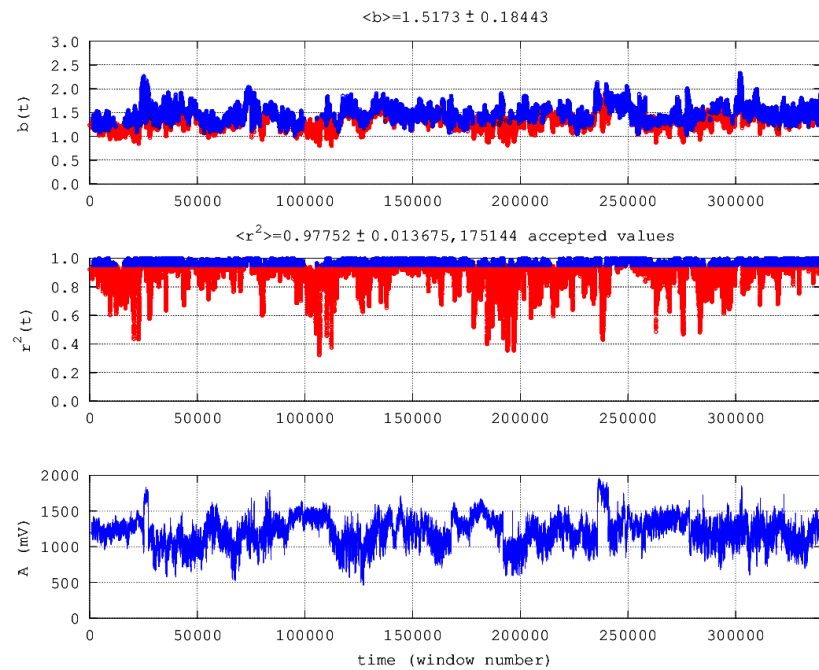


(a) Frequency 3 kHz—EW antenna orientation

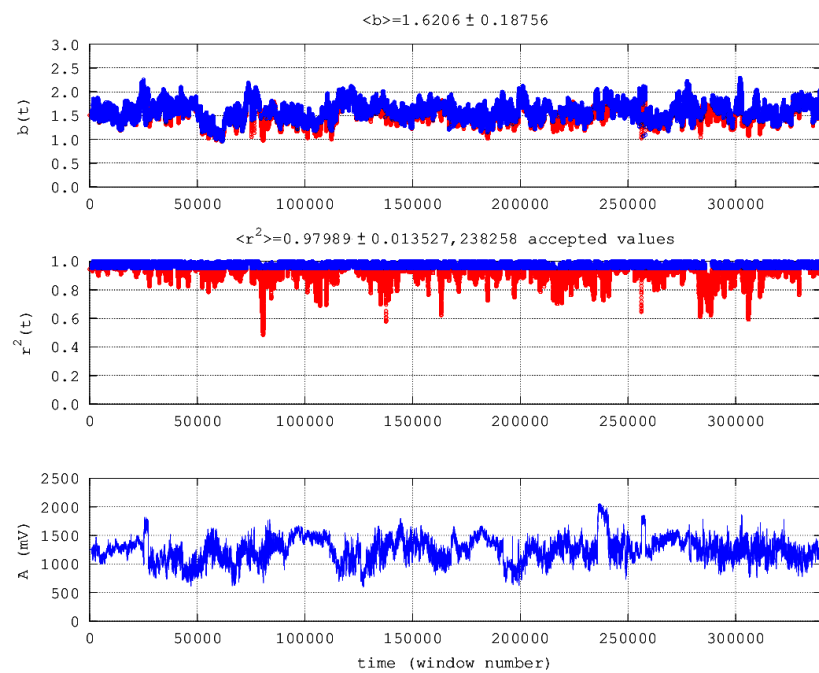


(b) Frequency 3 kHz—NS antenna orientation

Figure 4. Results from power-law analysis. Year 2018, 3 kHz EM observations from JD 185 to JD 188 (EQ2 occurred on JD 188, Table 1). From bottom to top: **(bottom)** The EM observations of amplitude A ; **(middle)** The square of Spearman’s correlation coefficient (r^2) in every 1024 window; **(top)** The evolution of power-law b -exponent ($b(t)$). The horizontal axis is measured in window number starting from the beginning of measurements (JD = 185, time = 00:00:00). Last window is omitted. The number of each window coincides with the actual EM measurement time in s (Section 3.1.1, sliding of step 1). Blue areas are accurate fractals ($r^2 \geq 0.95$). Red areas are non-fractal. The averages of b ($\langle b \rangle$) and r^2 ($\langle r^2(t) \rangle$) in accurate fractal areas are given \pm the corresponding standard deviations.

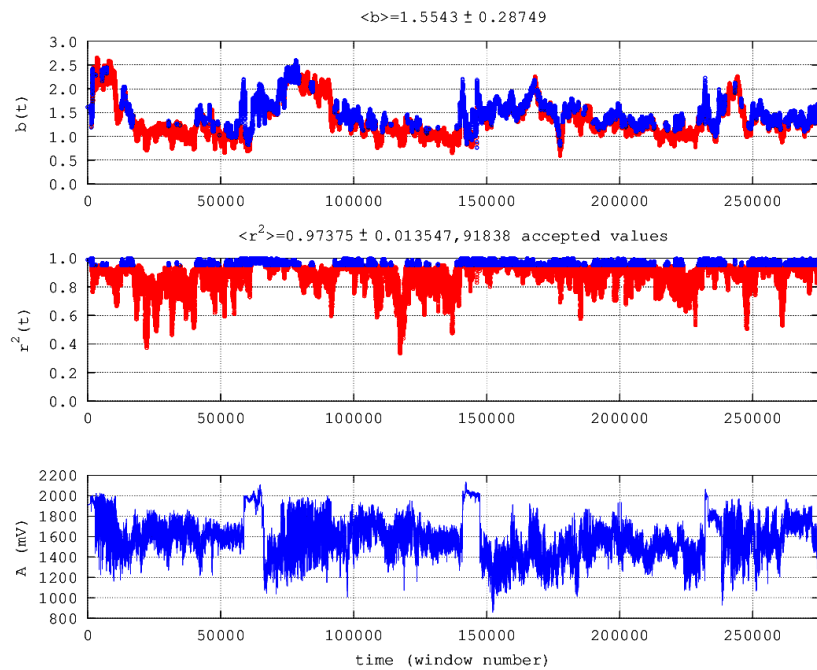


(a) Frequency 3 kHz—EW antenna orientation

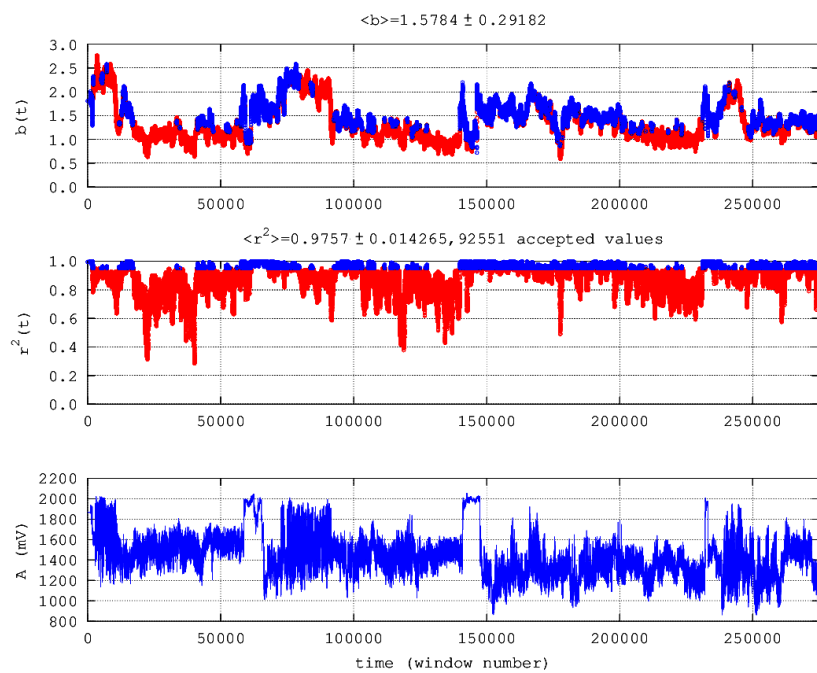


(b) Frequency 3 kHz—NS antenna orientation

Figure 5. Results from power-law analysis. Year 2015, 3 kHz EM observations from JD 239 to JD 242 (EQ3 occurred on JD 242, Table 1). From bottom to top: **(bottom)** The EM observations of amplitude A ; **(middle)** The square of Spearman’s correlation coefficient (r^2) in every 1024 window; **(top)** The evolution of power-law b -exponent ($b(t)$). The horizontal axis is measured in window number starting from the beginning of measurements (JD = 239, time = 00:00:00). Last window is omitted. The number of each window coincides with the actual EM measurement time in s (Section 3.1.1, sliding of step 1). Blue areas are accurate fractals ($r^2 \geq 0.95$). Red areas are non-fractal. The averages of b ($\langle b \rangle$) and r^2 ($\langle r^2(t) \rangle$) in accurate fractal areas are given \pm the corresponding standard deviations.

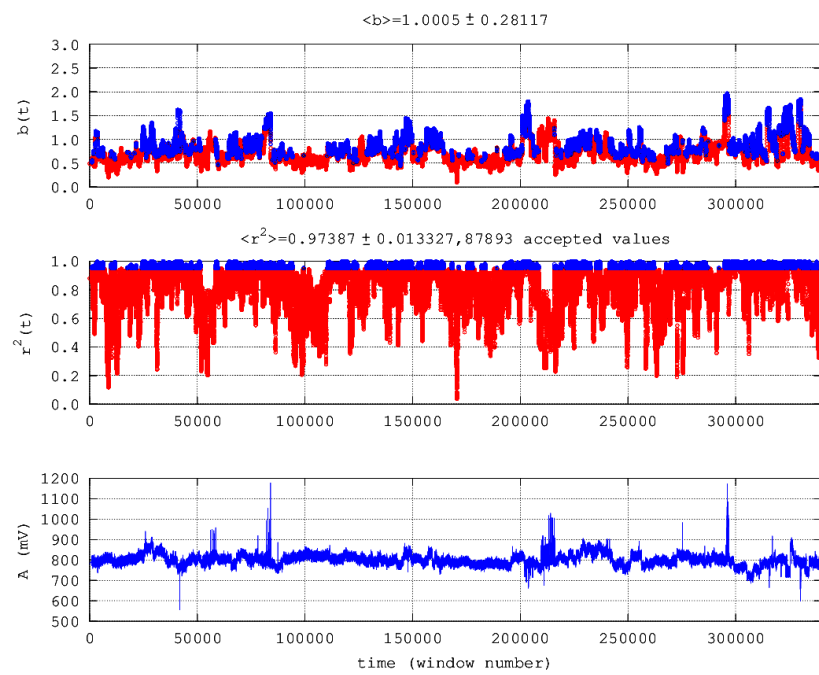


(a) Frequency 3 kHz—EW antenna orientation

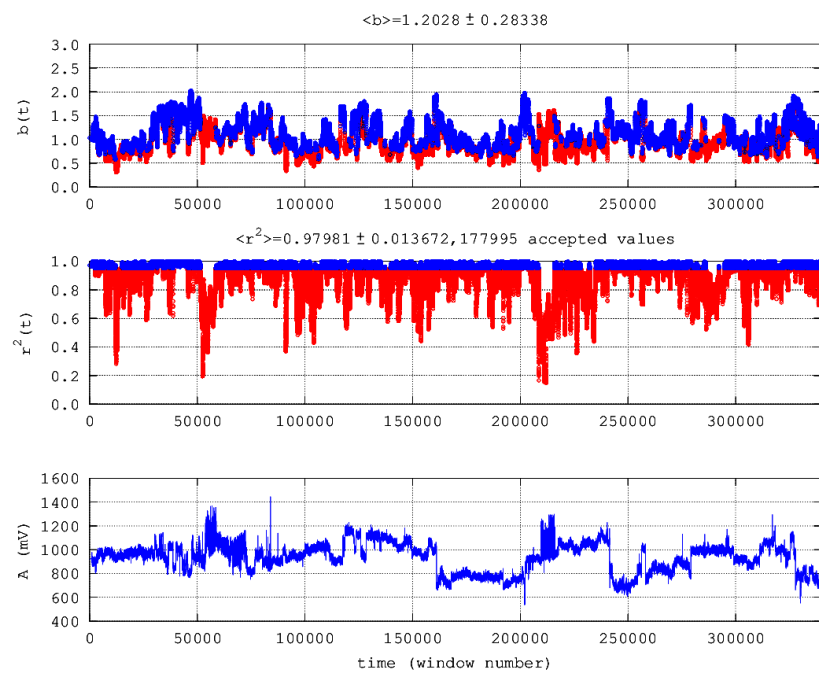


(b) Frequency 3 kHz—NS antenna orientation

Figure 6. Results from power-law analysis. Year 2015, 3 kHz EM observations from JD 343 to JD 346 (EQ3 occurred on JD 346, Table 1). From bottom to top: **(bottom)** The EM observations of amplitude A ; **(middle)** The square of Spearman’s correlation coefficient (r^2) in every 1024 window; **(top)** The evolution of power-law b -exponent ($b(t)$). The horizontal axis is measured in window number starting from the beginning of measurements (JD = 343, time = 00:00:00). Last window is omitted. The number of each window coincides with the actual EM measurement time in s (Section 3.1.1, sliding of step 1). Blue areas are accurate fractals ($r^2 \geq 0.95$). Red areas are non-fractal. The averages of b ($\langle b \rangle$) and r^2 ($\langle r^2(t) \rangle$) in accurate fractal areas are given \pm the corresponding standard deviations.

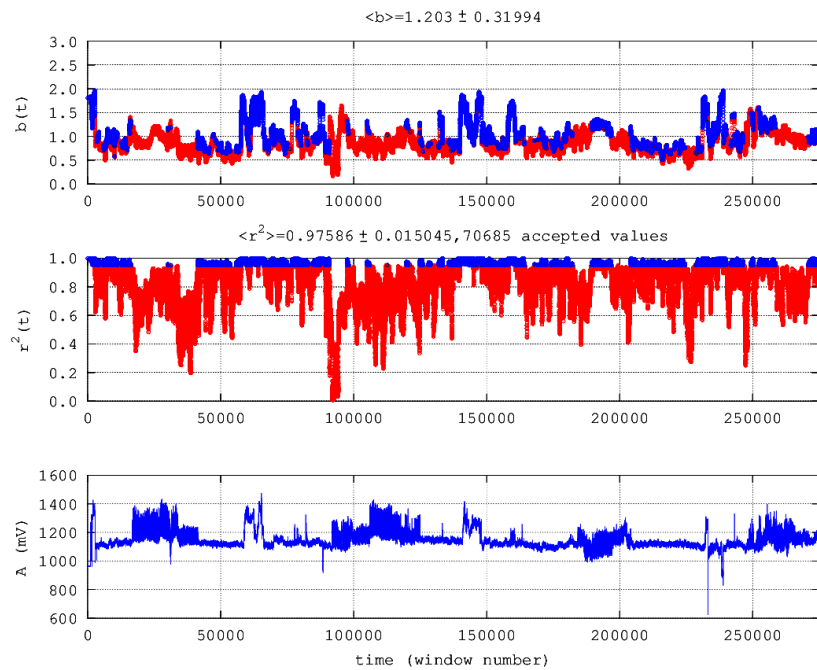


(a) Frequency 10 kHz—EW antenna orientation. EM observations from JD 239 to JD 242

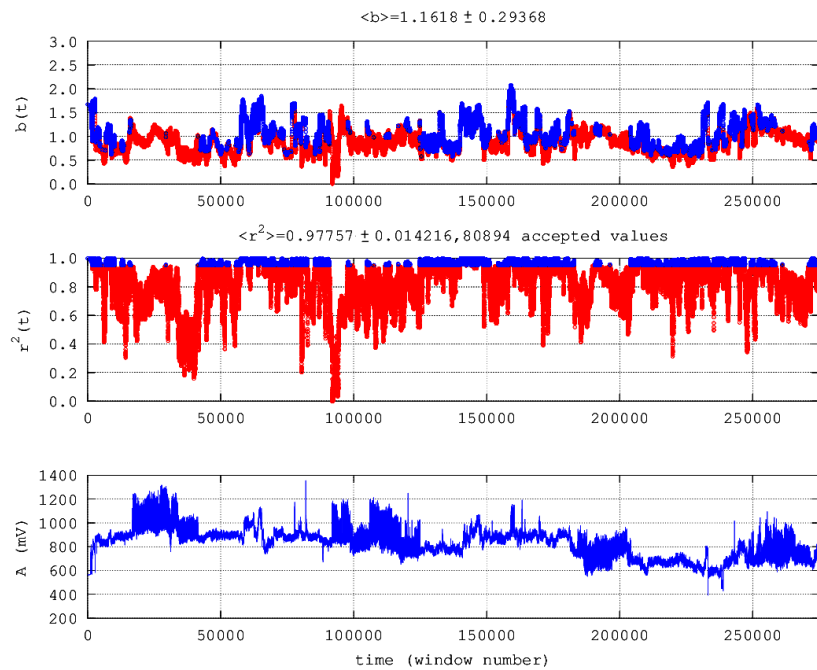


(b) Frequency 10 kHz—NS antenna orientation. Year 2015. EM observations from JD 239 to JD 242

Figure 7. Cont.



(c) Frequency 10 kHz—EW antenna orientation. Year 2015. EM observations from JD 343 to JD 346



(d) Frequency 10 kHz—NS antenna orientation. Year 2015. EM observations from JD 343 to JD 346

Figure 7. Results from power-law analysis. Year 2015, 10 kHz EM observations. EQ3 occurred on JD 242 and EQ4 on JD 346 (Table 1). From bottom to top: **(bottom)** The EM observations of amplitude A ; **(middle)** The square of Spearman’s correlation coefficient (r^2) in every 1024 window; **(top)** The evolution of power-law b -exponent ($b(t)$). The horizontal axis is measured in window number starting from the beginning of measurements (JD = 31, time = 00:00:00). Last window is omitted. The number of each window coincides with the actual EM measurement time in s (Section 3.1.1, sliding of step 1). Blue areas are accurate fractals ($r^2 \geq 0.95$). Red areas are non-fractal. The averages of b ($\langle b \rangle$) and r^2 ($\langle r^2(t) \rangle$) in accurate fractal areas are given \pm the corresponding standard deviations.

Table 2 presents the overall results from the power-law analysis. By observing Figures 3–7, a differentiation between blue and red areas can be marked, namely between accurate ($r^2 \geq 0.95$) fractal segments and non-accurate fractal segments. For the reader, it should be emphasised that the vast majority of blue areas, are also Class I segments and, as a result, the above differentiation is reflected also in the relation between the Class I and Class II segments of Table 2. Cases with much more Class I areas are those with $i/i = 1$ (Figure 3a), $i/i = 2$ (Figure 3b) and $i/i = 7$ (Figure 5b). Cases with more Class I segments are those with $i/i = 4$ (Figure 4a), with $i/i = 5$ (Figure 4b) and $i/i = 6$ (Figure 5a). All of these refer to the 3 kHz antennas' observations. Identifying more Class I segments is a first sign, but it is far from being considered enough for a precursory activity. The issues have been analysed extensively in previous publications ([27,29,31,35,87], and references therein). As pointed out in these references and mentioned above, the precursory significance, at least from the pure power-law analysis viewpoint, is the relation between the various b values. According to the aspects expressed in publications ([16,26,51,67,68,91–93], and references therein) as regards to the results of the power-law analysis, for sufficient and enough conditions to signalise the inevitable occurrence of ensuing earthquakes, is to identify in kHz antennas' persistent segments with power-law $b > 2$. According to these papers, the identification of kHz anomalies with $b > 2$ implies that the earthquake will occur from hours to days. Accounting to these aspects, the number of fractal persistent segments with $2 < b \leq 3$ gain significance. From this viewpoint, except from $i/i = 8$ (Figure 7a), $i/i = 9$ (Figure 7b) and $i/i = 12$ (Figure 7c), all other EM observations present fractal traces that can be considered as footprints of the related earthquakes, from the results of the power-law analysis and the viewpoint of the above publications. From the viewpoints expressed in previous publications ([27,29,31,35], and references therein), of importance for the precursory activity of ensuing earthquakes, are also the antipersistence-persistence interchanges with $1.7 \leq b < 2.3$. The reader should note here that the segments with $1.7 \leq b < 2.3$ include also segments that have $b > 2$. It is very interesting, according to this point of view, that all EM observations gave a significant number of areas with $1.7 \leq b < 2.3$, with the exception $i/i = 8$ (Figure 7a). The very strict criterion, however, of $2.3 \leq b \leq 3$ is covered only by the power-law analysis of five EM observations, namely $i/i = 1$ (Figure 3a), $i/i = 2$ (Figure 3b), $i/i = 3$ (Figure 3c), $i/i = 10$ (Figure 6a) and $i/i = 11$ (Figure 6b). Especially the latter two cases have many segments within this range. According to the evidence presented so far, the 3 kHz antennas are more efficient in presenting hidden pre-seismic fractal traces as derived from the power-law analysis from the EM observations. The 10 kHz antennas also present pre-earthquake signs but the fractal observations of (Figure 7) are of lesser importance.

Fractal patterns hidden within EM observations of the 3 kHz frequency have been found before the occurrence of other earthquakes in Greece (up to several days) [30,35]. Similar observations have been reported for MHz EM observations in Greece ([31,32,94], and references therein) and for pre-seismic radon in soil variations ([29,95], and references therein) and, importantly, with similar methodology. As discussed elsewhere [29,31,51], there is no one-to-one correspondence between certain observed activity and an ensuing earthquake. This is a limitation of the present methodology. Nevertheless, the fact that the studied earthquakes were very near the Ilia station and that numerous fractal trends were identified within a very close day window, make the results very important. This is a very significant advantage of the present analysis.

Table 2. Power-law analysis of the investigated earthquakes per antenna configuration. Abbreviations: (1) EQ1-EQ4: the corresponding earthquake of the analysis; (2) Antenna: the receiver frequency and configuration of the EM observations; (3) Class-I and Class-II: the number of segments per category; (4) Year of dataset (5) Julian Days of analysis within each year; (6) Figure that presents the data; (7) s.fGn: accurate fGn class; (8) s.fBm: accurate fBm class; (9): S: Stationary segment; (10) R: Random segment; (11) P: Persistent segment; (12) A: Antipersistent segment;

i/i	EQ	Antenna	Class II s.fGn		S $-1 \leq b < 1$	Class I s.fBm						Y	JD	Figure
			Class I	Class II		A $b = 1$	R $1 < b < 2$	P $b = 2$	A-P $2 < b \leq 3$	P $1.7 \leq b < 2.3$	P $2.3 \leq b \leq 3$			
1.	EQ1	3 kHz EW	200,813	78,055	3595	0	183,584	0	17,229	97,594	1490	2019	031-035	Figure 3a
2.		3 kHz NS	186,757	92,111	2362	0	180,131	0	6626	9004	30	2019	031-035	Figure 3b
3.		10 kHz EW	67,124	211,744	59,194	0	61,811	0	5313	8774	593	2019	031-035	Figure 3c
4.	EQ2	3 kHz EW	197,361	121,569	5800	0	191,726	0	5635	65,278	0	2018	185-188	Figure 4a
5.		3 kHz NS	194,585	124,345	6254	0	190,822	0	3762	59,609	6	2018	185-188	Figure 4b
6.	EQ3	3 kHz EW	173,415	165,282	1729	1	173,061	0	353	10,991	0	2015	239-242	Figure 5a
7.		3 kHz NS	238,076	100,621	182	0	235,567	0	2509	53,489	0	2015	239-242	Figure 5b
8.		10 kHz EW	10,479	328,218	77,414	0	10,479	0	0	0	0	2015	239-242	Figure 7a
9.		10 kHz NS	86,099	252,598	91,896	1	86,084	0	14	14,502	0	2015	343-346	Figure 7b
10.	EQ4	3 kHz EW	78,503	195,490	13,335	0	55,423	1	23,079	11,271	94,200	2015	343-346	Figure 6a
11.		3 kHz NS	81,335	192,658	11,216	0	56,278	0	25,057	25,995	8495	2015	343-346	Figure 6b
12.		10 kHz EW	19,176	254,817	51,509	0	19,176	0	0	3450	0	2015	343-346	Figure 7c
13.		10 kHz NS	26,471	247,522	54,423	0	126,471	0	80,891	693	0	2015	343-346	Figure 7d

According to the given analysis and the presented evidence, the majority of the *kHz* EM observations of this paper indicated that all earthquakes in Table 2 demonstrated distinctive characteristic epochs of fractal organisation in space and time. Since fractal organisation and long-term associations are so closely related, in the manner that one provides the other [35], the above epochs are also indicative of the long memory of the underlying geo-system. As mentioned in several parts of the text, the characteristic epochs of fractal organisation and long-term associations are consistent with the SOC states of the final preparation phase of the studied earthquakes ([29,95], and references therein). As expressed in several publications ([26,27,31,51,68], and references therein). These epochs were treated in this paper as pre-seismic warnings according to the given references. These characteristic pre-seismic epochs can be explained under the view of the asperity model [68]. According to this model, the focal area of the earthquakes in Table 2, consist of (i) a backbone of strong and large asperities distributed along the fault activated during the earthquake preparation process and (ii) a strongly heterogeneous medium, including weaker areas and smaller asperities that surround the family of main asperities. The heterogeneous medium sustains the system and the EM observations are modelled as fBm profiles. Throughout this phase, microcracks are distributed in the highly heterogeneous medium of the focal area. The microcracks develop continually into bigger fractures and the small fractures operate as small imitations of bigger ones, thus creating efficient channels for the spread of pre-seismic EM disturbances [35]. Importantly, this operation is the main property of fractality. Throughout this phase, critical Class I fBm-profiles are found [68]. However, when critical persistent and strong antipersistent-persistent variations occur, the conquering of the asperities begin. Thereafter, the fracture begins and the unavoidable evolution of the processes starts towards global failure. In this way, critical pre-seismic warnings are emitted, which were revealed in this paper with the fractal methods from the presented EM observations.

5. Conclusions

The main subject of this paper was the power-law analysis of *kHz* EM variations recorded by a station located in Kardamas, Iliia, Greece. EM variations were collected a few days prior to four earthquakes occurring within a 24 km radius around the Kardamas station. The epicentral depths of these earthquakes were below 29 km and, prior to the analysis, all EM observations gave indications of noteworthy visual variations, hence justifying the further analysis with fractals. All *kHz* EM observations revealed many fractal patterns. Many periods were found with hidden fractal traces corresponding to the predictable Class I fBm category exhibiting b exponents in the range $1 \leq b \leq 3$ ($0 \leq H \leq 1$). Non-precursory Class II segments were also addressed. Several analysed *kHz* EM segments were found to be persistent in the range $2 < b \leq 3$ ($0.5 < H \leq 1$). According to several papers, this finding is a significant sign of the impending earthquakes which were expected from days to hours prior to each event. This fact was deemed as significant and emphasised because of the short day window prior to the earthquakes that occurred. Numerous segments were found with strong persistent b -values in the range $2.3 \leq b \leq 3$ ($0.65 \leq H \leq 1$) or with b -values corresponding to switching between antipersistence and persistency with ($1.7 \leq b < 2.3$) ($0.35 \leq H < 0.65$). According to the literature, these were considered as very significant indications of the pre-seismic activity prior to the four earthquakes of this paper. The paper reports a table showing the number of segments per different b -value category which quantified the overall results from the power-law analysis. The findings from the power-law analysis from the *kHz* EM observations provided evidence that these observations were pre-earthquake signs of the four studied earthquakes. The results from the analysis were interpreted according to the asperity model of the preparation of earthquakes.

Author Contributions: Conceptualization, D.N.; Data curation, D.N., E.P. and D.C.; Formal analysis, D.N., E.P., M.R., A.A. and P.Y.; Investigation, D.N., M.R., A.A., P.Y. and D.C.; Methodology, D.N., E.P., M.R. and A.A.; Resources, D.N.; Software, D.N. and D.C.; Supervision, D.N. and E.P.; Visualization, D.N.; Writing—original draft, D.N. and D.C.; Writing—review and editing, D.N., E.P., P.Y., M.R., A.A. and D.C. All authors have read and agreed to the published version of the manuscript.

Funding: This research received no external funding.

Data Availability Statement: Data can be provided upon request.

Conflicts of Interest: The authors declare no conflict of interest.

References

1. Cicerone, R.; Ebel, J.; Britton, J. A systematic compilation of earthquake precursors. *Tectonophysics* **2009**, *476*, 371–396. [\[CrossRef\]](#)
2. Hough, S. *The Great Quake Debate: The Crusader, the Skeptic, and the Rise of Modern Seismology*; University of Washington Press: Seattle, WA, USA, 2020.
3. Hayakawa, M.; Hobara, Y. Current status of seismo-electromagnetics for short-term earthquake prediction. *Geomat. Nat. Hazards Risk* **2010**, *1*, 115–155. [\[CrossRef\]](#)
4. Molchanov, O.A.; Hayakawa, M. *Seismo-Electromagnetics and Related Phenomena: History and Latest Results*; Number A8; Terrapub: Tokyo, Japan, 2008; p. 189.
5. Ouzounov, D.; Pulinets, S.; Hattori, K.; Taylor, P. *Pre-Earthquake Processes: A Multidisciplinary Approach to Earthquake Prediction Studies Posters*; Wiley John Wiley and Sons: Hoboken, NJ, USA, 2018; p. 384.
6. Petraki, E.; Nikolopoulos, D.; Nomicos, C.; Stonham, J.; Cantzos, D.; Yannakopoulos, P.; Kottou, S. Electromagnetic Pre-earthquake Precursors: Mechanisms, Data and Models-A Review. *J. Earth Sci. Clim. Chang.* **2015**, *6*, 250. [\[CrossRef\]](#)
7. Petraki, E.; Nikolopoulos, D.; Panagiotaras, D.; Cantzos, D.; Yannakopoulos, P.; Nomicos, C.; Stonham, J. Radon-222: A Potential Short-Term Earthquake Precursor. *J. Earth Sci. Clim. Chang.* **2015**, *6*, 282. [\[CrossRef\]](#)
8. Uyeda, S.; Nagao, T.; Kamogawa, M. Short-term earthquake prediction: Current status of seismo-electromagnetics. *Tectonophysics* **2009**, *470*, 205–213. [\[CrossRef\]](#)
9. Conti, L.; Picozza, P.; Sotgiu, A. A Critical Review of Ground Based Observations of Earthquake Precursors. *Front. Earth Sci.* **2021**, *9*, 676766. [\[CrossRef\]](#)
10. Joshi, S.; Madhusudhanarao, K. Ultra-Low Frequency Geomagnetic Variations before Dholavira Earthquake M = 5.1 on the 20th of June 2012 in Kachchh Region, Gujarat, India. *Geotectonics* **2021**, *55*, 633–645. [\[CrossRef\]](#)
11. Bulusu, J.; Arora, K.; Singh, S.; Edara, A. Simultaneous electric, magnetic and ULF anomalies associated with moderate earthquakes in Kumaun Himalaya. *Nat. Hazards* **2023**, *116*, 3925–3955. [\[CrossRef\]](#)
12. Hayakawa, M.; Itoh, T.; Hattori, K.; Yumoto, K. ULF electromagnetic precursors for an earthquake at Biak, Indonesia on February 17, 1996. *Geophys. Res. Lett.* **2000**, *27*, 1531–1534. [\[CrossRef\]](#)
13. Hayakawa, M. VLF/LF radio sounding of ionospheric perturbations associated with earthquakes. *Sensors* **2007**, *7*, 1141–1158. [\[CrossRef\]](#)
14. Ida, Y.; Yang, D.; Li, Q.; Sun, H.; Hayakawa, M. Fractal analysis of ULF electromagnetic emissions in possible association with earthquakes in China. *Nonlin. Processes Geophys.* **2012**, *19*, 577–583. [\[CrossRef\]](#)
15. Ida, Y.; Hayakawa, M. Fractal analysis for the ULF data during the 1993 Guam earthquake to study prefracture criticality. *Nonlin. Processes Geophys.* **2012**, *13*, 409–412. [\[CrossRef\]](#)
16. Kaporis, P.; Peratzakis, J.P.A.; Nomikos, K.; Eftaxias, K. VHF-electromagnetic evidence of the underlying pre-seismic critical stage. *Earth Planets Space* **2002**, *54*, 1237–1246. [\[CrossRef\]](#)
17. Sarlis, N.; Skordas, E.; Varotsos, P.; Nagao, T.; Kamogawa, M.; Tanaka, H.; Uyeda, S. Minimum of the order parameter fluctuations of seismicity before major earthquakes in Japan. *Proc. Natl. Acad. Sci. USA* **2013**, *110*, 13734–13738. [\[CrossRef\]](#) [\[PubMed\]](#)
18. Skordas, E.S. On the increase of the “non-uniform” scaling of the magnetic field variations before the M(w)9.0 earthquake in Japan in 2011. *Chaos* **2014**, *24*, 023131. [\[CrossRef\]](#) [\[PubMed\]](#)
19. Smirnova, N.A.; Kiyashchenko, D.A.; Troyan, N.V.; Hayakawa, M. Multifractal Approach to Study the Earthquake Precursory Signatures Using the Ground-Based Observations. *Rev. Appl. Phys.* **2013**, *2*, 3.
20. Smirnova, N.; Hayakawa, M. Fractal characteristics of the ground-observed ULF emissions in relation to geomagnetic and seismic activities. *J. Atmos. Sol. Ter. Phys.* **2007**, *69*, 1833–1841. [\[CrossRef\]](#)
21. Varotsos, P.; Alexopoulos, K. Physical properties of the variations of the electric field of the earth preceding earthquakes, I. *Tectonophysics* **1984**, *110*, 73–98. [\[CrossRef\]](#)
22. Varotsos, P.; Alexopoulos, K. Physical properties of the variations of the electric field of the earth preceding earthquakes, II. *Tectonophysics* **1984**, *110*, 99–125. [\[CrossRef\]](#)
23. Varotsos, P.; Sarlis, N.; Skordas, E. Magnetic field variations associated with SES. The instrumentation used for investigating their detectability. *Proc. Jpn. Acad. Ser. B* **2001**, *77*, 87–92. [\[CrossRef\]](#)
24. Varotsos, P.; Sarlis, N.; Skordas, E. Long-range correlations in the electric signals that precede rupture: Further investigations. *Phys. Rev. E* **2003**, *67*, 021109. [\[CrossRef\]](#)

25. Varotsos, P.; Sarlis, N.; Skordas, E.; Lazaridou, M. Electric pulses some minutes before earthquake occurrences. *Appl. Phys. Lett.* **2007**, *90*, 064104. [[CrossRef](#)]
26. Eftaxias, K.; Balasis, G.; Contoyiannis, Y.; Papadimitriou, C.; Kalimeri, M. Unfolding the procedure of characterizing recorded ultra low frequency, kHz and MHz electromagnetic anomalies prior to the L'Aquila earthquake as pre-seismic ones—Part 2. *Nat. Hazards Earth Syst. Sci.* **2010**, *10*, 275–294. [[CrossRef](#)]
27. Cantzos, D.; Nikolopoulos, D.; Petraki, E.; Yannakopoulos, P.H.; Nomicos, C. Earthquake precursory signatures in electromagnetic radiation measurements in terms of day-to-day fractal spectral exponent variation: Analysis of the eastern Aegean 13/04/2017–20/07/2017 seismic activity. *J. Seismol.* **2018**, *22*, 1499–1513. [[CrossRef](#)]
28. Nikolopoulos, D.; Petraki, E.; Cantzos, D.; Yannakopoulos, P.H.; Panagiotaras, D.; Nomicos, C. Fractal Analysis of Pre-Seismic Electromagnetic and Radon Precursors: A Systematic Approach. *J. Earth Sci. Clim. Chang.* **2016**, *7*, 1–11.
29. Nikolopoulos, D.; Matsoukas, C.; Yannakopoulos, P.H.; Petraki, E.; Cantzos, D.; Nomicos, C. Long-Memory and Fractal Trends in Variations of Environmental Radon in Soil: Results from Measurements in Lesvos Island in Greece. *J. Earth Sci. Clim. Chang.* **2018**, *9*, 1–11. [[CrossRef](#)]
30. Nikolopoulos, D.; Yannakopoulos, P.H.; Petraki, E.; Cantzos, D.; Nomicos, C. Long-Memory and Fractal Traces in kHz-MHz Electromagnetic Time Series Prior to the ML = 6.1, 12/6/2007 Lesvos, Greece Earthquake: Investigation through DFA and Time-Evolving Spectral Fractals. *J. Earth Sci. Clim. Chang.* **2018**, *9*, 1–15.
31. Petraki, E. Electromagnetic Radiation and Radon-222 Gas Emissions as Precursors of Seismic Activity. Ph.D. Thesis, Department of Electronic and Computer Engineering, Brunel University, London, UK, 2016.
32. Petraki, E.; Nikolopoulos, D.; Fotopoulos, A.; Panagiotaras, D.; Koulouras, G.; Zisos, A.; Nomicos, C.; Louizi, A.; Stonham, J. Self-organised critical features in soil radon and MHz electromagnetic disturbances: Results from environmental monitoring in Greece. *Appl. Radiat. Isotop.* **2013**, *72*, 39–53. [[CrossRef](#)]
33. Petraki, E.; Nikolopoulos, D.; Fotopoulos, A.; Panagiotaras, D.; Nomicos, C.; Yannakopoulos, P.; Kottou, S.; Zisos, A.; Louizi, A.; Stonham, J. Long-range memory patterns in variations of environmental radon in soil. *Anal. Methods* **2013**, *5*, 4010–4020. [[CrossRef](#)]
34. Nikolopoulos, D.; Cantzos, D.; Petraki, E.; Yannakopoulos, P.H.; Nomicos, C. Traces of long-memory in pre-seismic MHz electromagnetic time series-Part1: Investigation through the R/S analysis and time-evolving spectral fractals. *J. Earth Sci. Clim. Chang.* **2016**, *7*, 359. [[CrossRef](#)]
35. Nikolopoulos, D.; Petraki, E.; Yannakopoulos, P.H.; Priniotakis, G.; Voyiatzis, I.; Cantzos, D. Long-lasting patterns in 3 kHz electromagnetic time series after the ML = 6.6 earthquake of 2018-10-25 near Zakynthos, Greece. *Geosciences* **2020**, *10*, 235. [[CrossRef](#)]
36. Zong, J.; Tao, D.; Shen, X. Possible ELF/VLF Electric Field Disturbances Detected by Satellite CSES before Major Earthquakes. *Atmosphere* **2022**, *13*, 1394. [[CrossRef](#)]
37. Yonaiguchi, N.; Ida, Y.; Hayakawa, M.; Masuda, S. Fractal analysis for VHF electromagnetic noises and the identification of preseismic signature of an earthquake. *J. Atmos. Sol. Ter. Phys.* **2007**, *69*, 1825–1832. [[CrossRef](#)]
38. Balasis, G.; Daglis, I.; Papadimitriou, C.; Kalimeri, M.; Anastasiadis, A.; Eftaxias, K. Dynamical complexity in Dst time series using non-extensive Tsallis entropy. *Geophys. Res. Lett.* **2008**, *35*, 1–6. [[CrossRef](#)]
39. Smirnova, N.; Hayakawa, M.; Gotoh, K. Precursory behavior of fractal characteristics of the ULF electromagnetic fields in seismic active zones before strong earthquakes. *Phys. Chem. Earth* **2004**, *29*, 445–451. [[CrossRef](#)]
40. Varotsos, P.; Sarlis, N.; Skordas, E. Scale-specific order parameter fluctuations of seismicity in natural time before mainshocks. *Europhys. Lett.* **2011**, *96*, 59002. [[CrossRef](#)]
41. Varotsos, P.; Sarlis, N.; Skordas, E.S.; Christopoulos, G.; Lazaridou, M.S. Identifying the occurrence time of an impending mainshock: A very recent case. *Earthq. Sci.* **2015**, *8*, 215–222. [[CrossRef](#)]
42. Varotsos, P.; Sarlis, N.; Skordas, E. Identifying the occurrence time of an impending major earthquake: A review. *Earthq. Sci.* **2017**, *30*, 209–218. [[CrossRef](#)]
43. Varotsos, P.A.; Sarlis, N.V.; Skordas, E.S. Order Parameter and Entropy of Seismicity in Natural Time before Major Earthquakes: Recent Results. *Geosciences* **2022**, *12*, 225. [[CrossRef](#)]
44. Varotsos, P.A.; Sarlis, N.V.; Skordas, E.S.; Nagao, T.; Kamogawa, M.; Flores-Márquez, E.L.; Ramírez-Rojas, A.; Perez-Oregon, J. Improving the Estimation of the Occurrence Time of an Impending Major Earthquake Using the Entropy Change of Seismicity in Natural Time Analysis. *Geosciences* **2023**, *13*, 222. [[CrossRef](#)]
45. Jiang, F.; Chen, X.; Chen, C.C.; Chen, H.J. Relationship Between Seismic Electric Signals and Tectonics Derived from Dense Geoelectric Observations in Taiwan. *Pure Appl. Geophys.* **2020**, *177*, 441–454. [[CrossRef](#)]
46. Argunov, V.V.; Gotovcev, M.R. Study of Ionospheric Effects and Earthquake Precursors Using Radio Engineering Methods. *IOP Conf. Ser. Earth Environ. Sci.* **2021**, *720*, 012087. [[CrossRef](#)]
47. Thomas, J.E.; Ekanem, A.M.; George, N.J.; Akpan, A.E. Ionospheric perturbations: A case study of 2007 five major earthquakes using DEMETER data. *Acta Geophys.* **2023**, *71*, 1607–1618. [[CrossRef](#)]
48. Vesnin, A.; Yasyukevich, Y.; Perevalova, N.; Şentürk, E. Ionospheric Response to the 6 February 2023 Turkey&-Syria Earthquake. *Remote Sens.* **2023**, *15*, 2336. [[CrossRef](#)]
49. Nikolopoulos, D.; Moustiris, K.; Petraki, E.; Cantzos, D. Fractal and long-memory traces in PM₁₀ time series in Athens, Greece. *Environmetrics* **2019**, *6*, 29. [[CrossRef](#)]

50. Nikolopoulos, D.; Moustiris, K.; Petraki, E.; Cantzos, D. Long-memory traces in PM₁₀ time series in Athens, Greece: Investigation through DFA and R/S analysis. *Meteorol. Atmos. Phys.* **2021**, *133*, 261–279. [[CrossRef](#)]
51. Eftaxias, K.; Balasis, G.; Contoyiannis, Y.; Papadimitriou, C.; Kalimeri, M.; Athanasopoulou, L.; Nikolopoulos, S.; Kopanas, J.; Antonopoulos, G.; Nomicos, C. Unfolding the procedure of characterizing recorded ultra low frequency, kHz and MHz electromagnetic anomalies prior to the L'Aquila earthquake as pre-seismic ones-Part 1. *Nat. Hazard Earth Syst.* **2009**, *9*, 1953–1971. [[CrossRef](#)]
52. Gotoh, K.; Hayakawa, M.; Smirnova, N.; Hattori, K. Fractal analysis of seismogenic ULF emissions. *Phys. Chem. Earth* **2004**, *29*, 419–424. [[CrossRef](#)]
53. NOA. Available online: <https://www.gein.noa.gr/en/services-products/database-search/> (accessed on 11 August 2023).
54. Davis, G.H. Partitioned tectonic shortening, with emphasis on outcrop-scale folding and flattening, Pindos fold-and-thrust belt, Peloponnese, Greece. *Can. J. Earth Sci.* **2019**, *56*, 1181–1201. [[CrossRef](#)]
55. Skourlis, K.; Doutsos, T. The Pindos Fold-and-thrust belt (Greece): Inversion kinematics of a passive continental margin. *Int. J. Earth Sci.* **2003**, *92*, 891–903. [[CrossRef](#)]
56. Lekas, A.; Fountoulis, I.; Papanikolaou, D. Intensity Distribution and Neotectonic Macrostructure Pyrgos Earthquake Data (26 March 1993, Greece). *Nat. Hazards* **2000**, *21*, 19–33. [[CrossRef](#)]
57. USGS. Available online: <https://earthquake.usgs.gov/earthquakes/map/?extent=22.41103,91.51611&extent=35.56798,113.57666&range=search&baseLayer=terrain&timeZone=utc&search=> (accessed on 26 May 2023).
58. Mandelbrot, B.B.; Ness, J.W.V. Fractional Brownian motions, fractional noises and applications. *J. Soc. Ind. Appl. Math.* **1968**, *10*, 422–437. [[CrossRef](#)]
59. Morales, I.O.; Landa, O.; Fossion, R.; Frank, A. Scale invariance, self-similarity and critical behaviour in classical and quantum system. *J. Phys. Conf. Ser.* **2012**, *380*, 012020. [[CrossRef](#)]
60. Musa, M.; Ibrahim, K. Existence of long memory in ozone time series. *Sains Malays.* **2012**, *41*, 1367–1376.
61. Vadrevu, K.P. Fractal analysis revealed persistent correlations in long-term vegetation fire data in most South and Southeast Asian countries. *Environ. Res. Commun.* **2023**, *5*, 011001. [[CrossRef](#)]
62. May, R.M. Simple mathematical models with very complicated dynamics. *Nature* **1976**, *261*, 459–467. [[CrossRef](#)]
63. Sugihara, G.; May, R. Nonlinear forecasting as a way of distinguishing chaos from measurement error in time series. *Nature* **1990**, *344*, 734–741. [[CrossRef](#)]
64. Liu, C.; Liang, J.; Li, Y.; Shi, K. Fractal analysis of impact of PM_{2.5} on surface O₃ sensitivity regime based on field observations. *Sci. Total. Environ.* **2023**, *858*, 160136. [[CrossRef](#)]
65. Pastén, D.; Pavez-Orrego, C. Multifractal time evolution for intraplate earthquakes recorded in southern Norway during 1980–2021. *Chaos Solitons Fractals* **2023**, *167*, 113000. [[CrossRef](#)]
66. Chelidze, T.; Matcharashvili, T.; Mepharidze, E.; Dovgal, N. Complexity in Geophysical Time Series of Strain/Fracture at Laboratory and Large Dam Scales: Review. *Entropy* **2023**, *25*, 467. [[CrossRef](#)]
67. Kapiris, P.; Eftaxias, K.; Nomikos, K.; Polygiannakis, J.; Dologlou, E.; Balasis, G.; Bogris, N.; Peratzakis, A.; Hadjicontis, V. Evolving towards a critical point: A possible electromagnetic way in which the critical regime is reached as the rupture approaches. *Nonlinear Proc. Geoph.* **2003**, *10*, 1–14. [[CrossRef](#)]
68. Eftaxias, K.; Contoyiannis, Y.; Balasis, G.; Karamanos, K.; Kopanas, J.; Antonopoulos, G.; Koulouras, G.; Nomicos, C. Evidence of fractional-Brownian-motion-type asperity model for earthquake generation in candidate pre-seismic electromagnetic emissions. *Nat. Hazard Earth Syst.* **2008**, *8*, 657–669. [[CrossRef](#)]
69. Varotsos, P.A.; Sarlis, N.V.; Skordas, E.S. Attempt to distinguish electric signals of a dichotomous nature. *Phys. Rev. E* **2003**, *68*, 031106. [[CrossRef](#)] [[PubMed](#)]
70. Hurst, H. Long term storage capacity of reservoirs. *Trans. Am. Soc. Civ. Eng.* **1951**, *116*, 770–808. [[CrossRef](#)]
71. Hurst, H.; Black, R.; Simaiki, Y. *Long-Term Storage: An Experimental Study*; Constable: London, UK, 1965.
72. Lopez, T.; Martinez-Gonzalez, C.; Manjarrez, J.; Plascencia, N.; Balankin, A. Fractal Analysis of EEG Signals in the Brain of Epileptic Rats, with and without Biocompatible Implanted Neuroreservoirs. *Appl. Mech. Mater.* **2009**, *15*, 127–136. [[CrossRef](#)]
73. Kilcik, A.; Anderson, C.; Rozelot, J.; Ye, H.; Sugihara, G.; Ozguc, A. Nonlinear Prediction of Solar Cycle 24. *Astrophys. J.* **2009**, *693*, 1173–1177. [[CrossRef](#)]
74. Chattopadhyay, A.; Khondekar, M. An investigation of the relationship between the CME and the Geomagnetic Storm. *Astron. Comput.* **2023**, *43*, 100695. [[CrossRef](#)]
75. Dattatreya, G. Hurst Parameter Estimation from Noisy Observations of Data Traffic Traces. In Proceedings of the 4th WSEAS International Conference on Electronics, Control and Signal Processing, Rio de Janeiro, Brazil, 25–27 April 2005; pp. 193–198.
76. Wang, F.; Wang, H.; Zhou, X.; Fu, R. A Driving Fatigue Feature Detection Method Based on Multifractal Theory. *IEEE Sens. J.* **2022**, *22*, 19046–19059. [[CrossRef](#)]
77. Zhou, H.; Chang, F. The long-memory temporal dependence of traffic crash fatality for different types of road users. *Phys. A Stat. Mech. Appl.* **2022**, *607*, 128210. [[CrossRef](#)]
78. Rehman, S.; Siddiqi, A. Wavelet based Hurst exponent and fractal dimensional analysis of Saudi climatic dynamics. *Chaos Solitons Fractals* **2009**, *39*, 1081–1090. [[CrossRef](#)]
79. Li, X.; Polygiannakis, J.; Kapiris, P.; Peratzakis, A.; Eftaxias, K.; Yao, X. Fractal spectral analysis of pre-epileptic seizures in terms of criticality. *J. Neural Eng.* **2005**, *2*, 11–16. [[CrossRef](#)] [[PubMed](#)]

80. Escobar-Ipuz, F.; Torres, A.; García-Jiménez, M.; Basar, C.; Cascón, J.; Mateo, J. Prediction of patients with idiopathic generalized epilepsy from healthy controls using machine learning from scalp EEG recordings. *Brain Res.* **2023**, *1798*, 148131. [[CrossRef](#)]
81. Wijayanto, I.; Humairani, A.; Hadiyoso, S.; Rizal, A.; Prasanna, D.L.; Tripathi, S.L. Epileptic seizure detection on a compressed EEG signal using energy measurement. *Biomed. Signal Process. Control* **2023**, *85*, 104872. [[CrossRef](#)]
82. Granero, M.S.; Segovia, J.T.; Perez, J.G. Some comments on Hurst exponent and the long memory processes on capital Markets. *Physica A* **2008**, *387*, 5543–5551. [[CrossRef](#)]
83. Musaev, A.; Makshanov, A.; Grigoriev, D. The Genesis of Uncertainty: Structural Analysis of Stochastic Chaos in Finance Markets. *Complexity* **2023**, *2023*, 1302220. [[CrossRef](#)]
84. Pérez-Sienes, L.; Grande, M.; Losada, J.C.; Borondo, J. The Hurst Exponent as an Indicator to Anticipate Agricultural Commodity Prices. *Entropy* **2023**, *25*, 579. [[CrossRef](#)] [[PubMed](#)]
85. Vogl, M. Hurst exponent dynamics of S&P 500 returns: Implications for market efficiency, long memory, multifractality and financial crises predictability by application of a nonlinear dynamics analysis framework. *Chaos Solitons Fractals* **2023**, *166*, 112884. [[CrossRef](#)]
86. Fujinawa, Y.; Takahashi, K. Electromagnetic radiations associated with major earthquakes. *Phys. Earth Planet Inter.* **1998**, *105*, 249–259. [[CrossRef](#)]
87. Alam, A.; Wang, N.; Petraki, E.; Barkat, A.; Huang, F.; Shah, M.A.; Cantzos, D.; Priniotakis, G.; Yannakopoulos, P.H.; Papoutsidakis, M.; et al. Fluctuation Dynamics of Radon in Groundwater Prior to the Gansu Earthquake, China (22 July 2013: Ms = 6.6): Investigation with DFA and MF DFA Methods. *Pure Appl. Geophys.* **2021**, *178*, 3375–3395. [[CrossRef](#)]
88. Telesca, L.; Lasaponara, R. Vegetational patterns in burned and unburned areas investigated by using the detrended fluctuation analysis. *Physica A* **2006**, *368*, 531–535. [[CrossRef](#)]
89. Morgounov, V. Relaxation creep model of impending earthquake. *Ann. Geophys.* **2001**, *44*, 369–381. [[CrossRef](#)]
90. Varotsos, P.A.; Sarlis, N.V.; Skordas, E.S. Self-organized criticality and earthquake predictability: A long-standing question in the light of natural time analysis. *Europhys. Lett.* **2020**, *132*, 29001. [[CrossRef](#)]
91. Contoyiannis, Y.; Kaporis, P.; Eftaxias, K. Monitoring of a preseismic phase from its electromagnetic precursors. *Phys. Rev. E* **2005**, *71*, 066123. [[CrossRef](#)] [[PubMed](#)]
92. Minadakis, G.; Potirakis, S.; Nomicos, C.; Eftaxias, K. Linking electromagnetic precursors with earthquake dynamics: An approach based on nonextensive fragment and self-affine asperity models. *Physica A* **2012**, *391*, 2232–2244. [[CrossRef](#)]
93. Papadimitriou, C.; Kalimeri, M.; Eftaxias, K. Nonextensivity and universality in the earthquake preparation process. *Phys. Rev. E* **2008**, *77*, 036101. [[CrossRef](#)]
94. Cantzos, D.; Nikolopoulos, D.; Petraki, E.; Nomicos, C.; Yannakopoulos, P.H.; Kottou, S. Identifying Long-Memory Trends in Pre-Seismic MHz Disturbances through Support Vector Machines. *J. Earth. Sci. Clim. Chang.* **2015**, *6*, 1–9.
95. Nikolopoulos, D.; Petraki, E.; Marousaki, A.; Potirakis, S.; Koulouras, G.; Nomicos, C.; Panagiotaras, D.; Stonhamb, J.; Louizi, A. Environmental monitoring of radon in soil during a very seismically active period occurred in South West Greece. *J. Environ. Monit.* **2012**, *14*, 564–578. [[CrossRef](#)]

Disclaimer/Publisher’s Note: The statements, opinions and data contained in all publications are solely those of the individual author(s) and contributor(s) and not of MDPI and/or the editor(s). MDPI and/or the editor(s) disclaim responsibility for any injury to people or property resulting from any ideas, methods, instructions or products referred to in the content.